Electronic Supplementary Material (ESI) for Energy & Environmental Science.

Supplementary Information

Probing the Stability of $SrIrO_3$ During Active Water Electrolysis via Operando Atomic Force Microscopy

Andrew R. Akbashev,[1,2,3] Vladimir Roddatis,[4] Christoph Baeumer,[1,2,5] Tianchi Liu,[1] J. Tyler Mefford,[1,2] William C. Chueh[1,2]

[1]Department of Materials Science and Engineering, Stanford University, Stanford, CA 94305, USA.
[2]Stanford Institute for Materials and Energy Sciences, SLAC National Accelerator Laboratory, Menlo Park, CA 94025, USA.
[3]Division for Research with Neutrons and Muons, Paul Scherrer Institute, 5232 Villigen, Switzerland
[4]German Research Centre for Geosciences GFZ, Helmholtz Centre Potsdam, 14473 Potsdam, Germany.
[5]Institute of Electronic Materials (IWE2) and JARA-FIT, RWTH Aachen University, 52062 Aachen, Germany.

* Corresponding authors: andrei.akbasheu@psi.ch

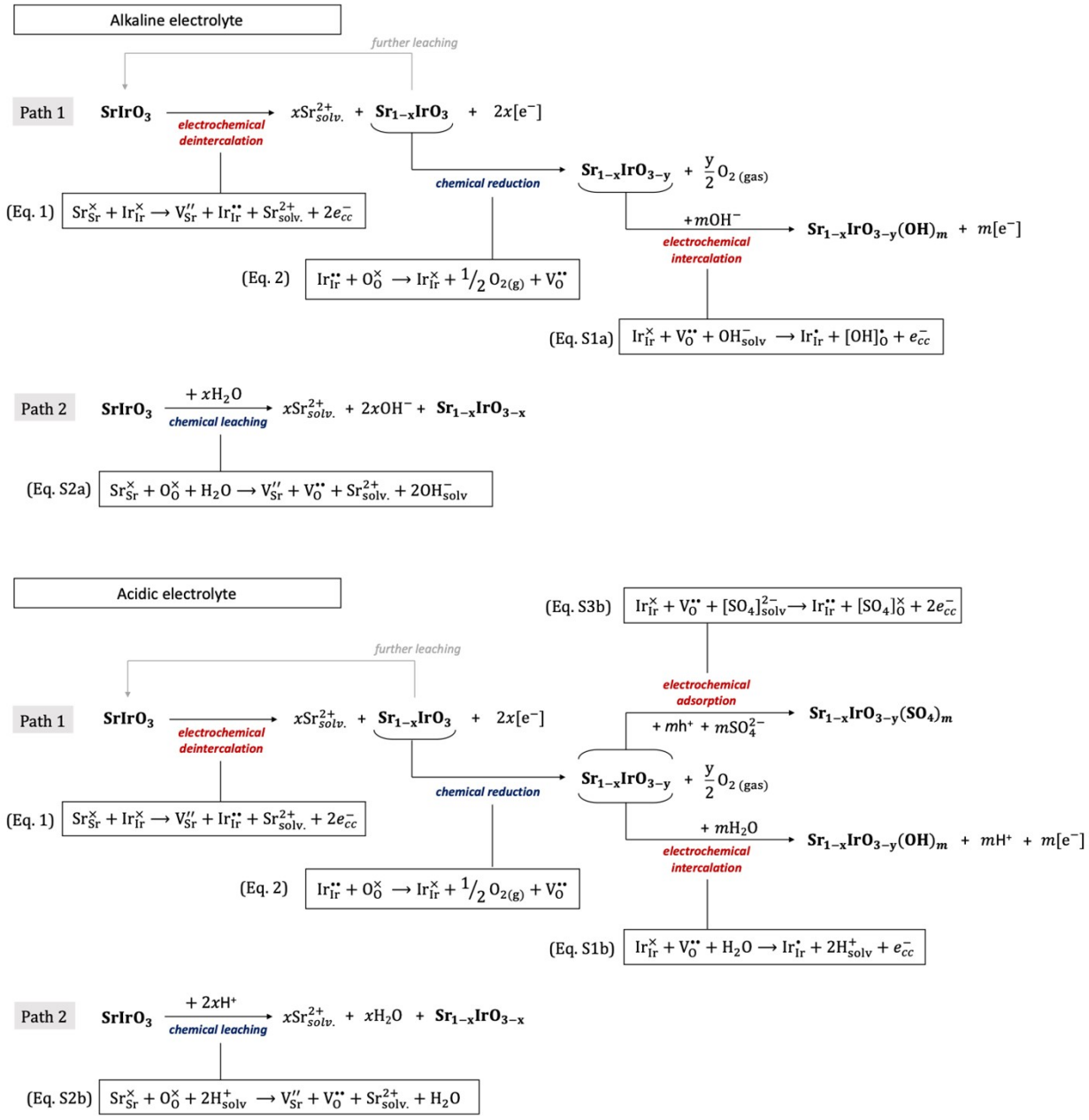

Equations S1. Possible mechanisms for Sr leaching from $SrIrO_3$ in alkaline (KOH) and acidic (H_2SO_4) media. "cc" stands for current collector; "solv" implies that the species is in the solution.

(a) "Path 1" is an electrochemical pathway. It starts with electrochemical de-insertion of Sr^{2+} (Eq. 1). The resulting $Sr_{1-x}IrO_3$ can be reduced chemically through oxygen loss to $Sr_{1-x}IrO_{3-y}$ (this reaction can happen electrochemically if the potential is reduced, for example during CV). The formation of oxyhydroxide within the surface region of $Sr_{1-x}IrO_{3-y}$ can happen through the electrochemical intercalation of OH^- (or formation of oxysulfate due to the electrochemical adsorption of SO_4^{2-}). Other, more complex, steps are also possible.

(b) "Path 2" is a chemical pathway. It involves leaching and dissolution of the Sr^{2+}-O^{2-} Schottky pairs.

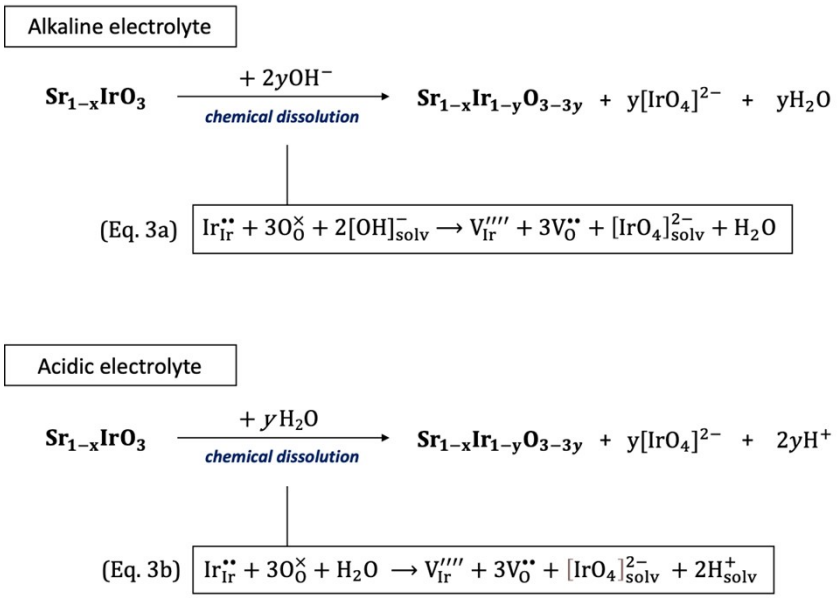

Equations S2. Possible mechanism for Ir dissolution for $SrIrO_3$ in the alkaline and acidic medium under highly oxidative OER conditions. This dissolution requires a highly oxidized Ir species such as Ir(VI) (Ir(V) may also be part of the process as it is also soluble) that forms electrochemically following one of the pathways in Equations 1.

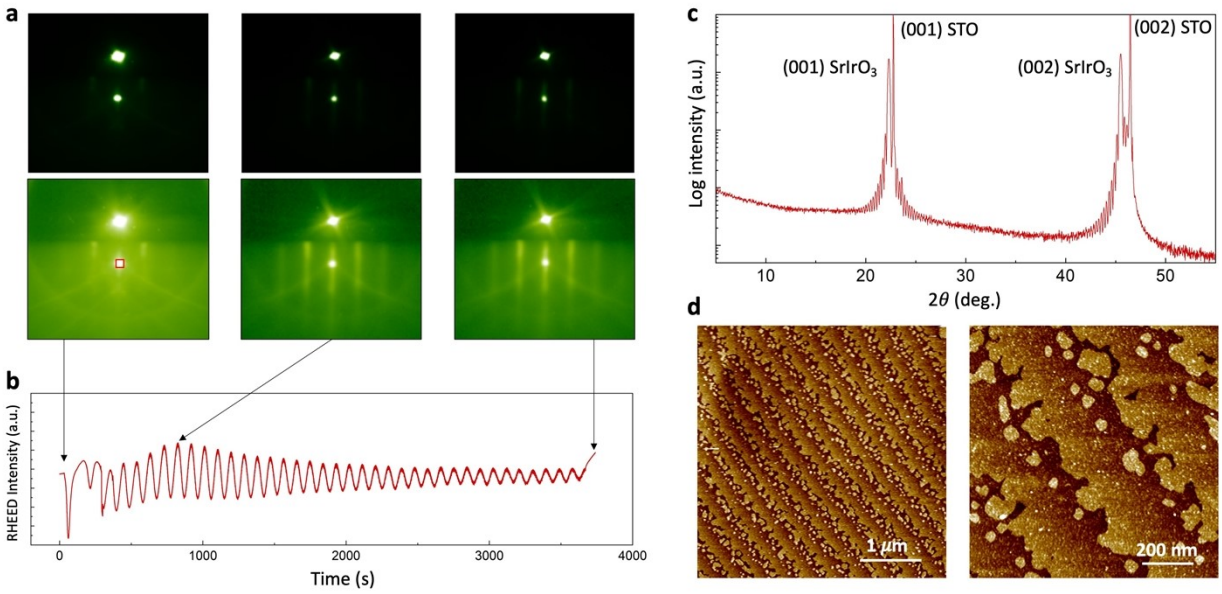

Figure S1. (a) RHEED patterns and (b) oscillations of the specular reflection during a well-optimized growth of (001) $SrIrO_3$. (c) X-ray diffraction of (001) $SrIrO_3$ on (001) Nb:$SrTiO_3$. (d) Topographic images (AFM) of the as-deposited $SrIrO_3$ film.

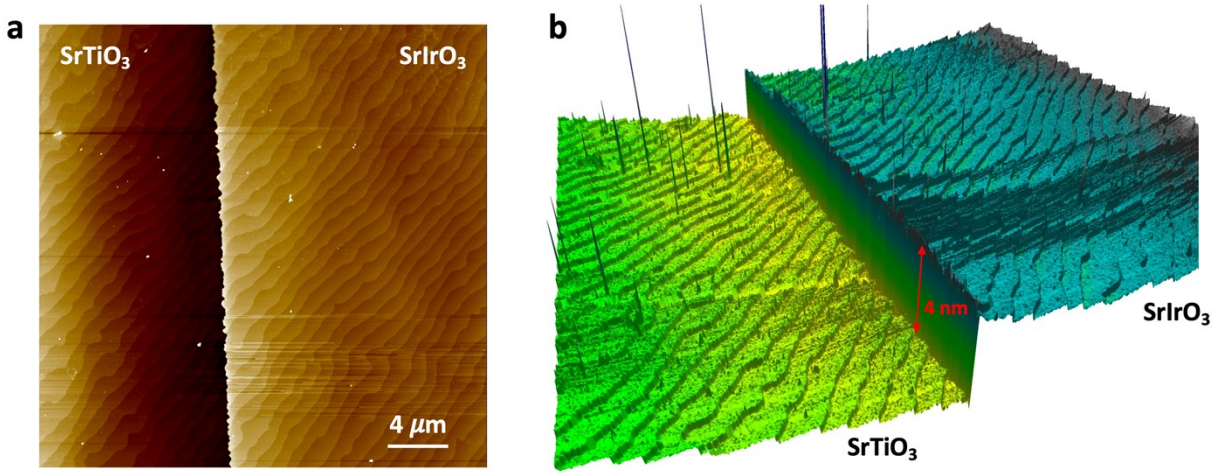

Figure S2. (a) The topographic image and (b) its 3D view of the step between the $SrIrO_3$ film and exposed $SrTiO_3$ substrate.

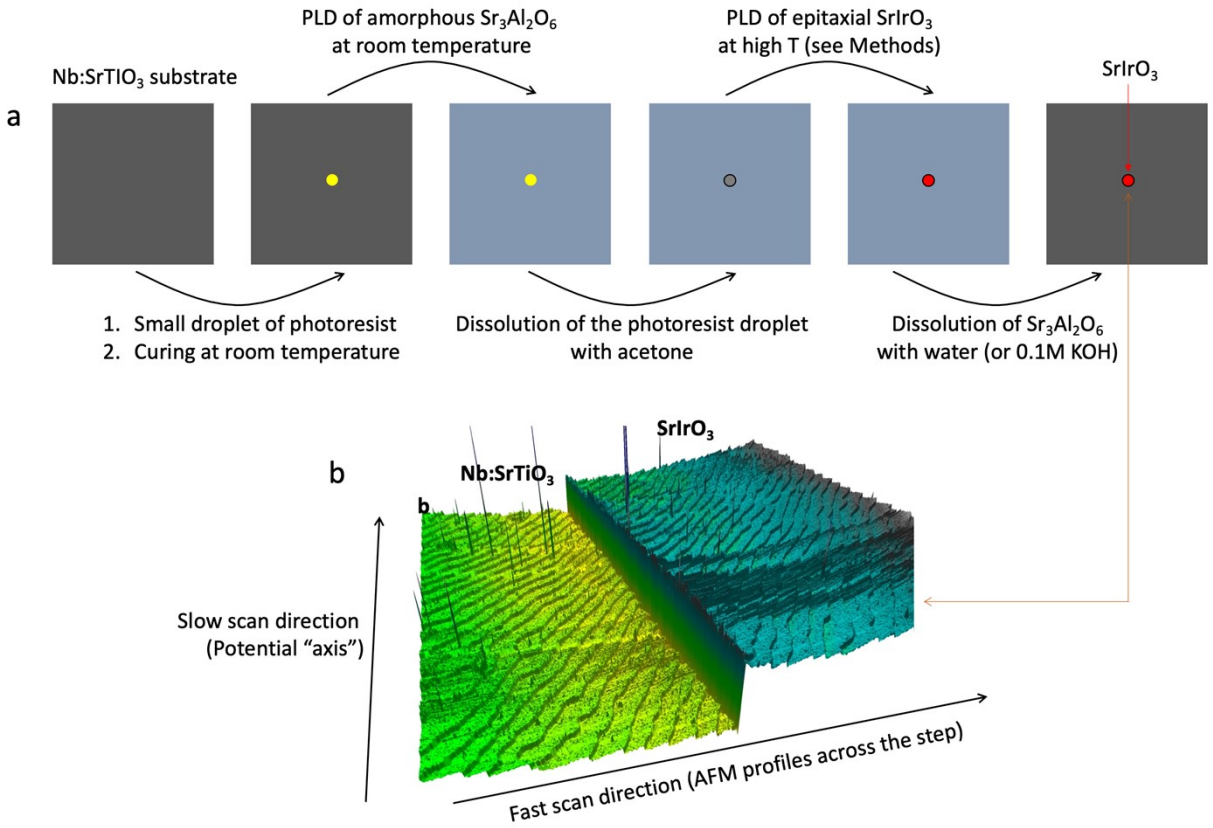

Figure S3. (a) The procedure used for the preparation of the step between the substrate ($Nb:SrTIO_3$) and the film ($SrIrO_3$). This approach also significantly reduced the size of the electrode area and made it easier to conduct the *operando* EC-AFM experiments. (b) The directions of the AFM scans: slow scanning is done along the step direction and is correlated with the applied potential while fast scanning is carried out perpendicular to the step and ensures the height of the film is recorded at each potential.

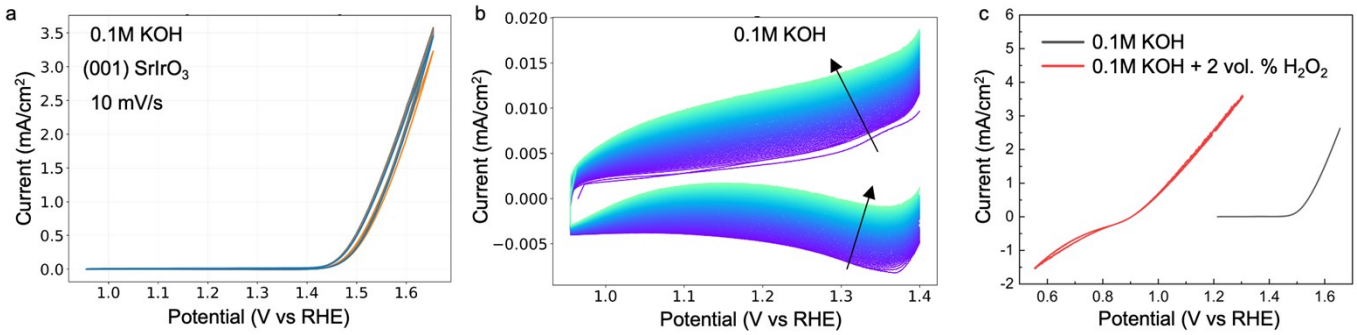

Figure S4. (a) Cyclic voltammetry sweeps measured for $SrIrO_3$ in 0.1M KOH (scan rate is 10 mV/s), with a total of 101 sweeps done. (b) The capacitive region before the OER onset (from (a)) showing a positive shift of the current with each cycle (black arrows). Most likely, this shift is due to the oxidation of the generated H_2O_2 that can form during water oxidation. This effect was observed on multiple samples. (c) An electrochemical response of $SrIrO_3$ in 0.1M KOH + 2 vol.% H_2O_2, demonstrating potentials similar to those in (b). No *iR* correction was made because our samples showed a potential-dependent solid-state junction resistance (see Methods).

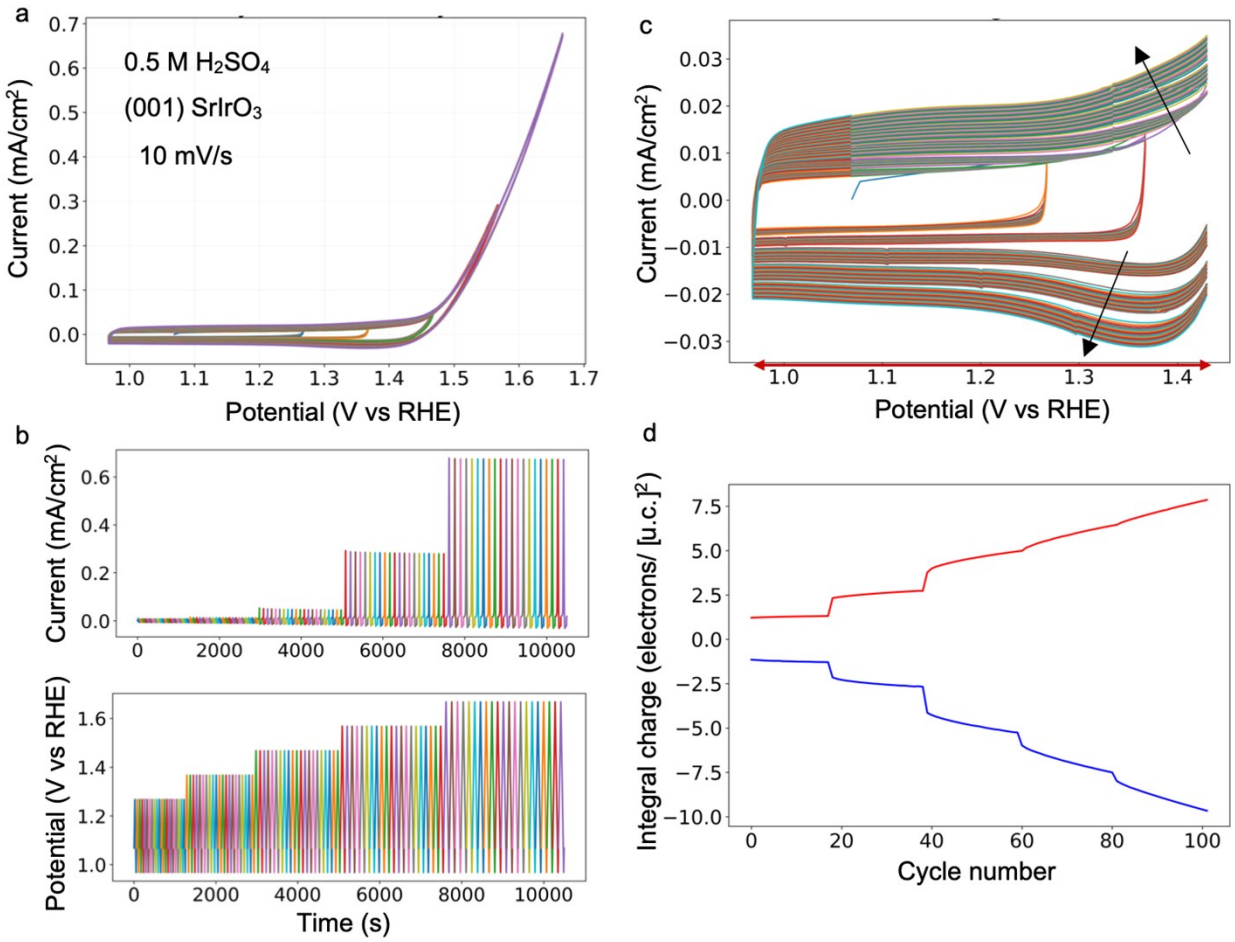

Figure S5. (a) Cyclic voltammetry sweeps measured for $SrIrO_3$ in 0.5M H_2SO_4 (scan rate is 10 mV/s). For each potential range a set of 21 sweeps are made. The time dependences of the current and potential are given in (b). (c) The capacitive region before the OER onset showing an increase in the capacitance both within the 21 sweeps and after each expansion of the potential window (black arrows). (d) The charge integrated for the potential range given by the red arrow in (c) and plotted as a function of the CV number. No *iR* correction was made because our samples showed a potential-dependent solid-state junction resistance (see Methods).

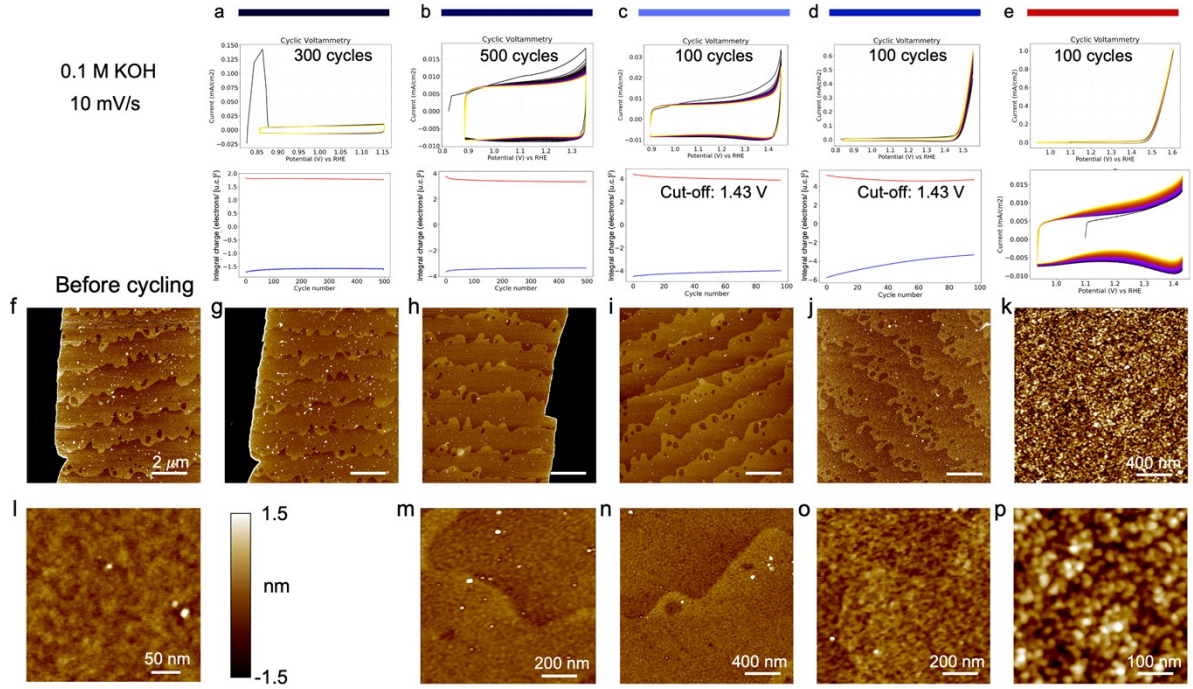

Figure S6. An *ex situ* experiment that involved CV measurements using the RDE, each followed by *ex situ* AFM scans of the dry sample. Color bars at the top of the figure correspond to the colored profiles in Figure S7. Electrochemical tests of the $SrIrO_3$ film were performed in 0.1M KOH. (a-e) (a-e) CV measurements and the integral charge for the anodic and cathodic direction up to the maximum applied potential or the cut-off potential. (g-k) The corresponding low-resolution AFM images (for (g-j) the scale bar is 2 um). (m-p) Higher resolution scans of (i-k). (f,l) The AFM scans of the as-prepared sample. The black region corresponds to the substrate.

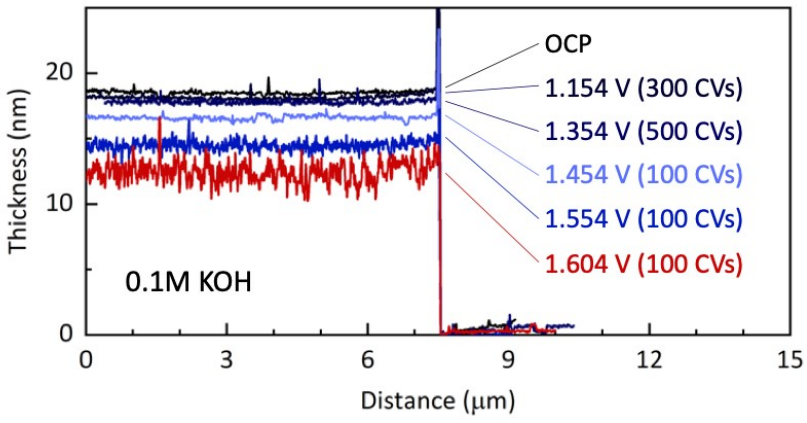

Figure S7. The height of $SrIrO_3$ film after cycling voltammetry experiments extracted from the data shown in Figure S6.

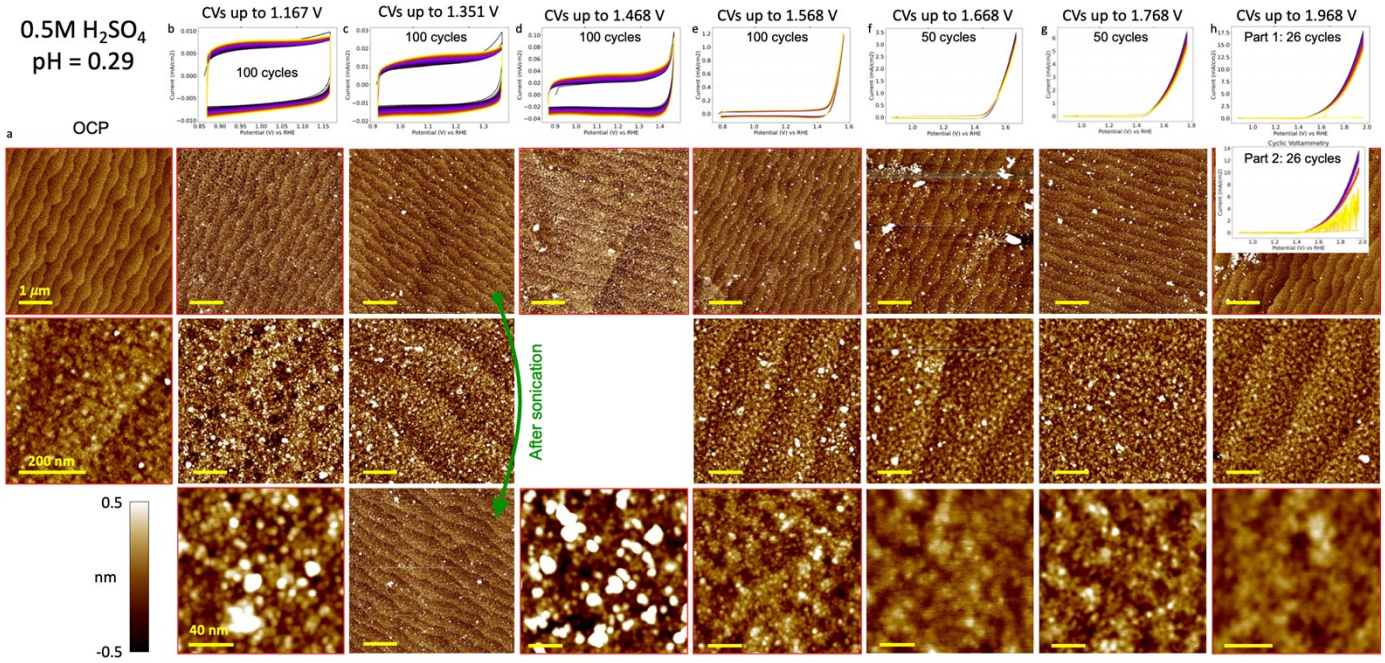

Figure S8. An *ex situ* experiment that involved the CV measurements using the RDE, each followed by *ex situ* AFM scans of the dry sample. In this case the electrochemical tests of the $SrIrO_3$ film were performed in 0.5M H_2SO_4. (a) AFM scans: each column corresponds to the scan after CV sweeps performed in RDE (except for the first column that represents the topography of the as-grown sample). The scale bars in each row are the same as in the first image of the row. Thus, the rows show the surface evolution with progressively more anodic cycling, while the columns show the enlarged area of the same surface. For the (c) row the sample was also mildly sonicated. First, the results show that during cycling the surface quickly develop islands and they cannot be removed by conventional sonication, which implies that the islands are part of the surface and are not simple redeposits. This point is further supported by the fact that they do not move during the AFM scan, which is normally not the case for loosely attached particles. Second, as the potential reaches OER, the surface becomes cleaner (less rough), although larger islands are still present. Finally, when the OER currents reach over 10 mA/cm^2, the surface becomes almost as clean as the initial (OCP) state.

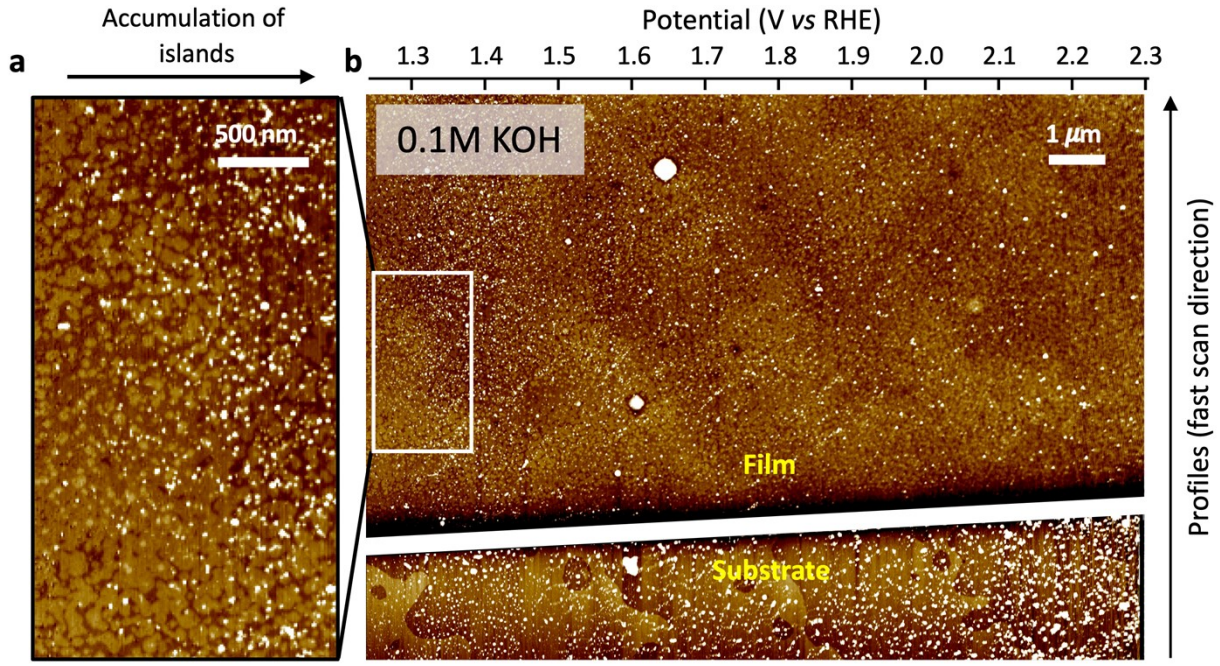

Figure S9. An *operando* EC-AFM measurement of the $SrIrO_3$ film in 0.1M KOH. (a) An enlarged region of the AFM image in (b) showing the appearance of islands on the surface without the loss of the step-terraced surface morphology. (b) AFM image acquired during a slow potential scan. The slow axis of the AFM scan is directed along the potential axis. The film and substrate areas in the scan are separately flattened and adjusted for the z-scale to ensure that both surfaces are clearly visible.

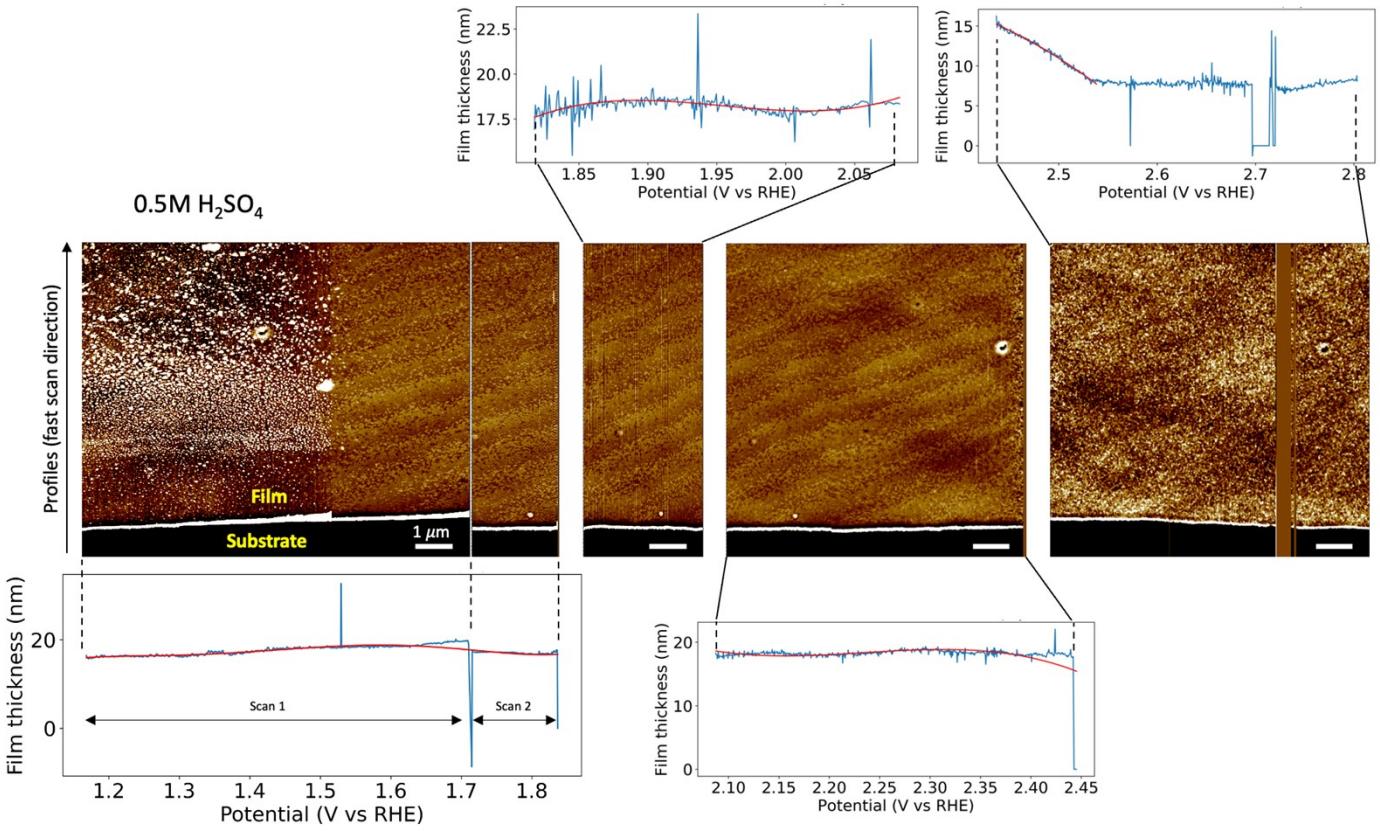

Figure S10. An *operando* EC-AFM measurement of the $SrIrO_3$ film in 0.5M H_2SO_4 (extended dataset for Figure 2d). All AFM images were acquired during a slow uninterrupted potential scan. The slow axis of the AFM scan is directed along the potential axis.

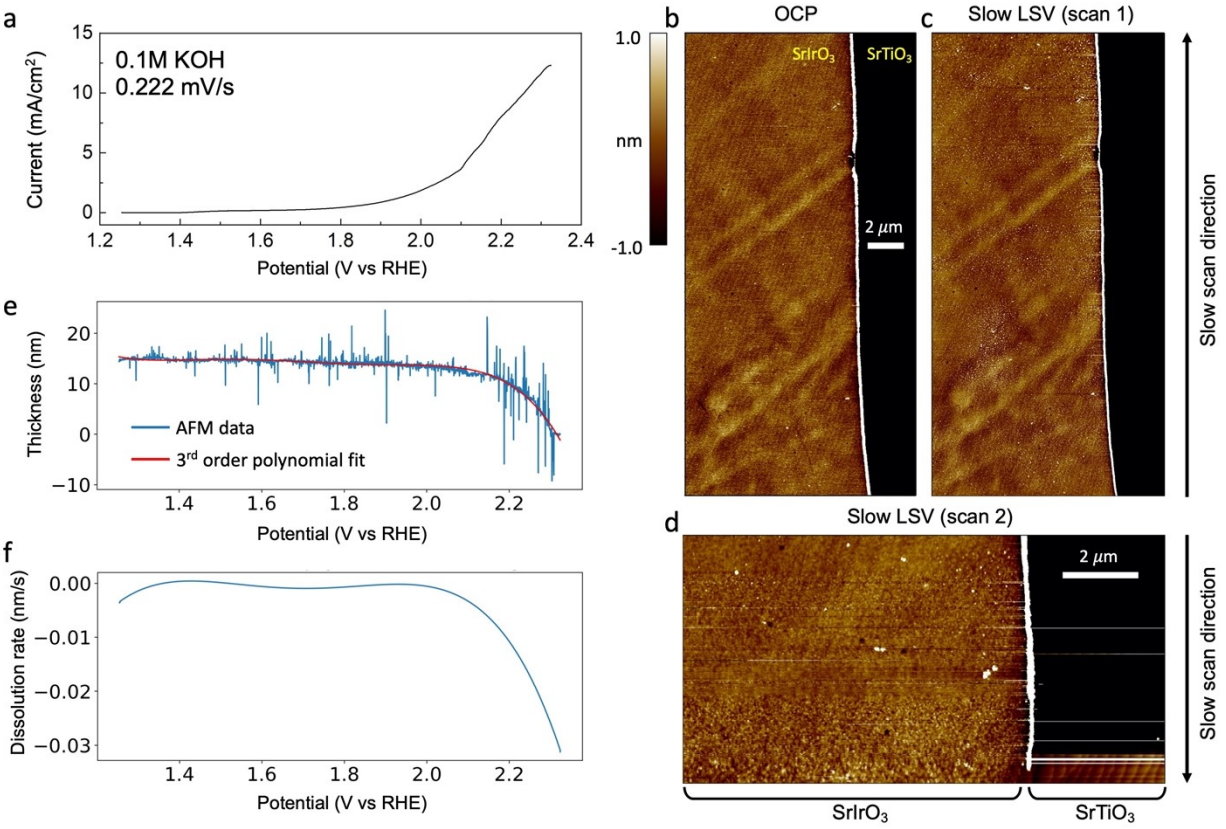

Figure S11. An *in-situ* AFM experiment during a slow LSV (0.222 mV/s) of a 15-nm thick $SrIrO_3$ film in 0.1M KOH. (a) The slow LSV scan. (b) The topographic image of the sample before the experiment (at open-circuit potential). The black region is the substrate. (c) The image of the sample during a slow LSV. In the end of the first AFM scan (scan 1) a new scan began (scan 2). Small islands can be observed at the surface. (d) The second AFM scan that shows a complete dissolution of the $SrIrO_3$ film in the end. Note that the slow scan direction is opposite for (c) and (d). The scan in (d) is a continuation of the scan in (c), but starting from the top of the area. (e) The evolution of the film thickness with potential extracted from (c) and (d). (f) The dissolution rate calculated as a derivative of the 3rd order polynomial shown in (e). The dissolution begins at ~ 2 V vs RHE and the rate quickly raises.

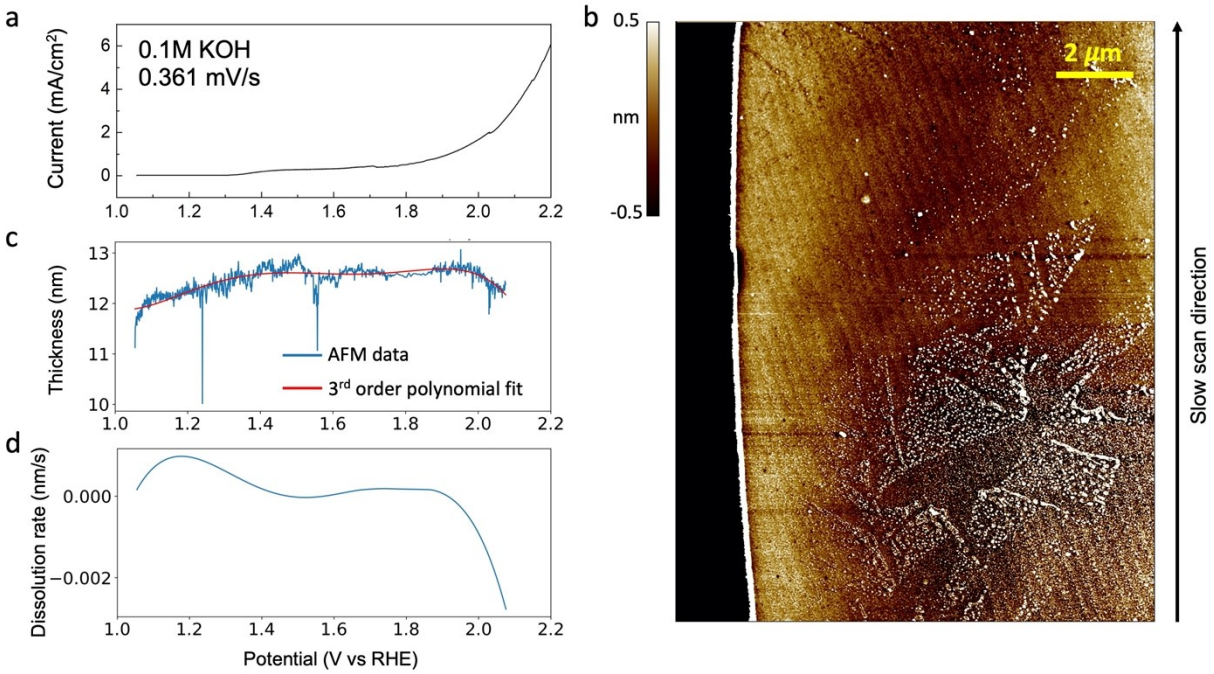

Figure S12. An *in-situ* AFM experiment during a slow LSV (0.361 mV/s) of the $SrIrO_3$ film in 0.1M KOH. (a) The slow LSV plot corresponding to the AFM image in (b). The AFM image shows the appearance of islands on the surface after the start of the scan. The islands induce a variation in thickness shown in (c). We did not reach the potential of active dissolution in this experiment due to the bubble formation.

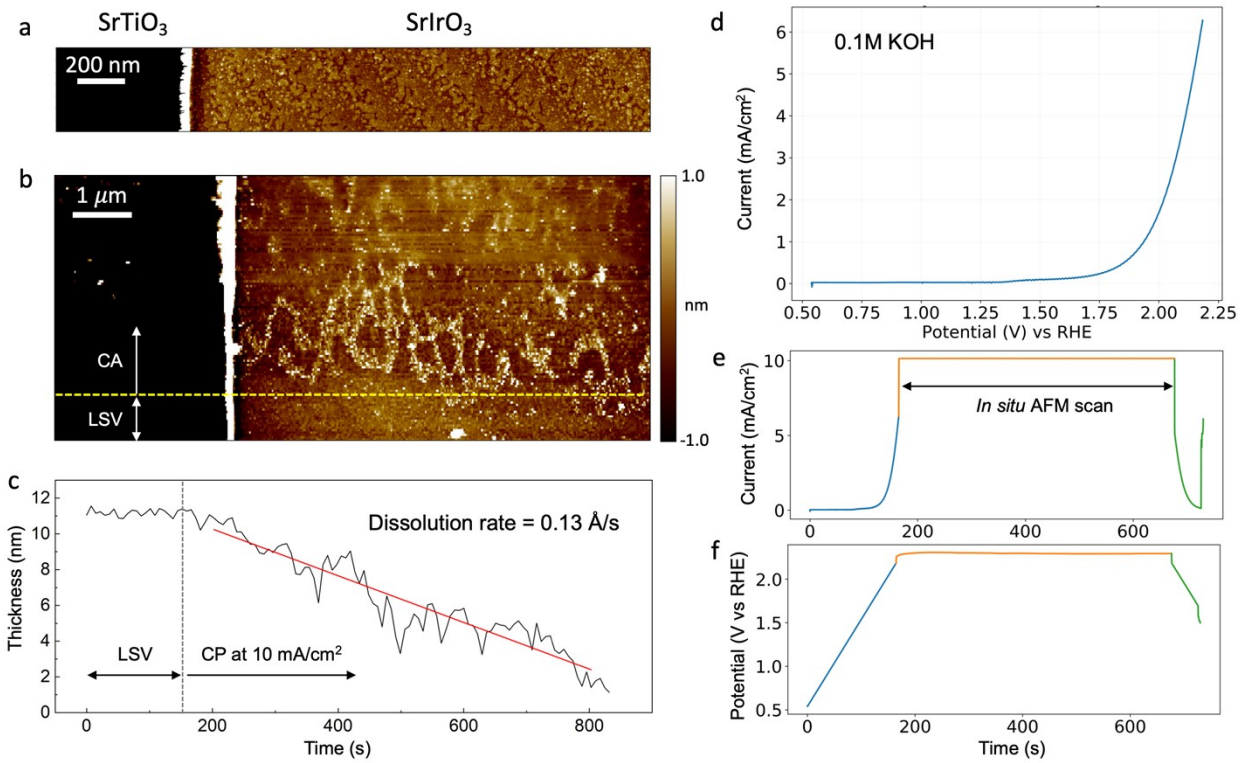

Figure S13. An *in-situ* AFM experiment during galvanostatic measurements (10 mA/cm^2) of a 12-nm thick $SrIrO_3$ film in 0.1M KOH. (a) The AFM scan of the initial step-terraced surface of the film. The dark part is the substrate region. (b) The slow AFM scan with the LSV region marked. The appearance of islands is seen as white streaks on the surface. (c) The height change during the initial potential increase and subsequent galvanostatic measurement. The dissolution rate is ~0.1 Å/s. (d) The initial LSV curve. (e-f) Time dependences of the current and potential during the measurements.

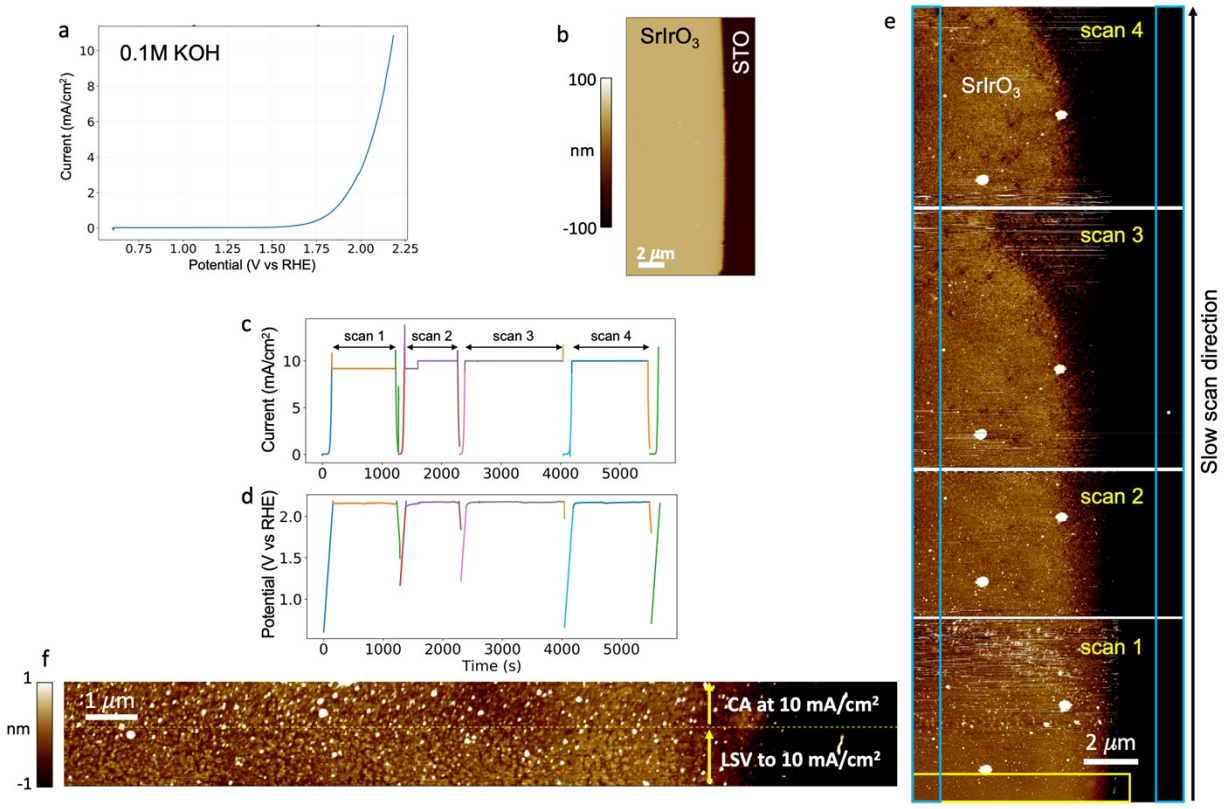

Figure S14. An *in-situ* AFM experiment during galvanostatic measurements (~10 mA/cm^2) of a 120-nm thick $SrIrO_3$ film in 0.1M KOH. (a) The CV of the sample recording inside the AFM. (b) AFM topography scan of the substrate-film edge at the open circuit potential (before *in-situ* measurements). (c-d) Time dependences of the current and potential during different separate AFM scans. In the first scan, the current was 9 mA/cm^2. Each AFM scan is started from the bottom of the same scanned region. The reason for multiple scans is the nucleation of oxygen bubbles despite a relatively high electrolyte flow (200-400 uL/min). (e) AFM scans collected *in-situ*: the blue rectangles show the regions used for the height extraction (one in the film and one in the substrate region). The direction of the slow scanning axis of the AFM is shown with the arrow on the right side. (f) The enlarged region of the scan 1 in (e) outlined by the yellow rectangle. This region shows the appearance of islands on step terraces after the current reaches ~9 mA/cm^2. The LSV region corresponds to the part of the scan during the linear voltage increase (up to 10.8 mV/s) to the value of the galvanostatic measurement.

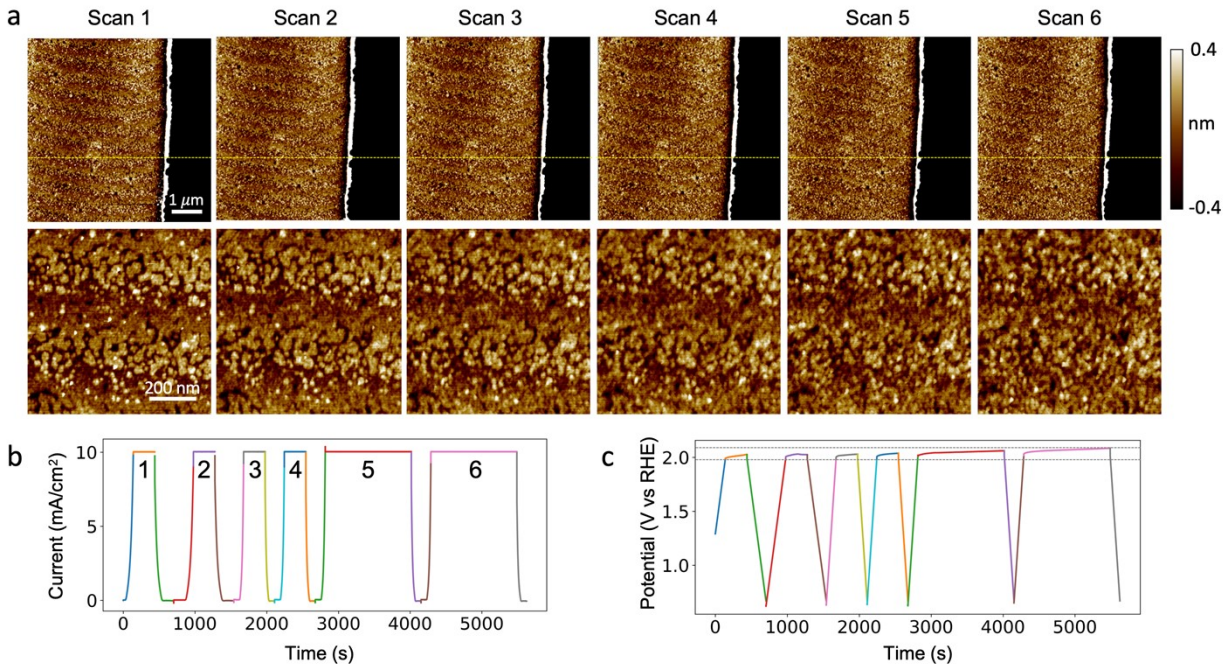

Figure S15. Topographic AFM scans performed after each galvanostatic measurement (10 mA/cm^2) of the $SrIrO_3$ film in 0.5M H_2SO_4. The black region in the top row of images is the substrate. The bottom row of images show the enlarged area of $SrIrO_3$ with step terraces. The time dependences of the current and potential are given in (b). The grey dashed lines in the lower plot in (b) show the initial and final potential after prolonged constant-current measurements. The thickness of the film stays constant within the time of the measurement, with a small increase in its surface roughness.

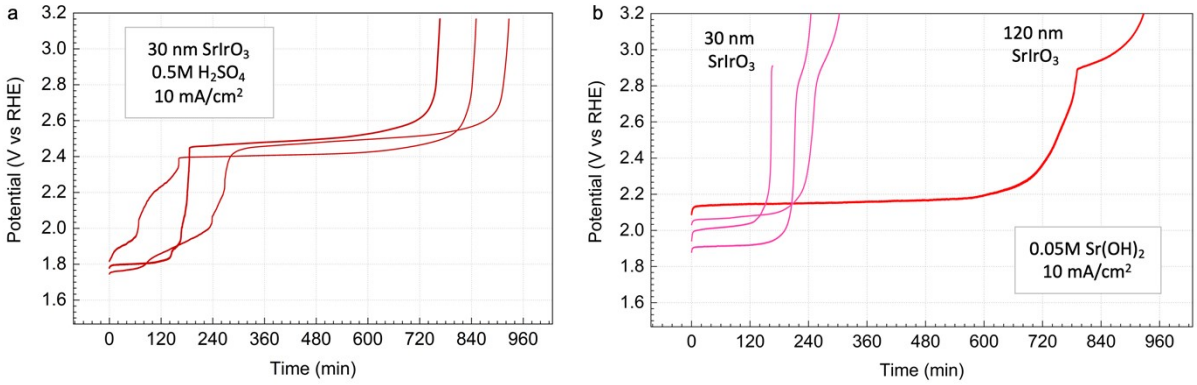

Figure S16. Galvanostatic experiments conducted on 30-nm $SrIrO_3$ films in the 0.5M H_2SO_4 and 0.05M $Sr(OH)_2$ electrolytes. The measurements show the sample-to-sample variation of the dissolution time. As all samples were grown under identical conditions, the reason for the different degradation time on the same samples is unknown.

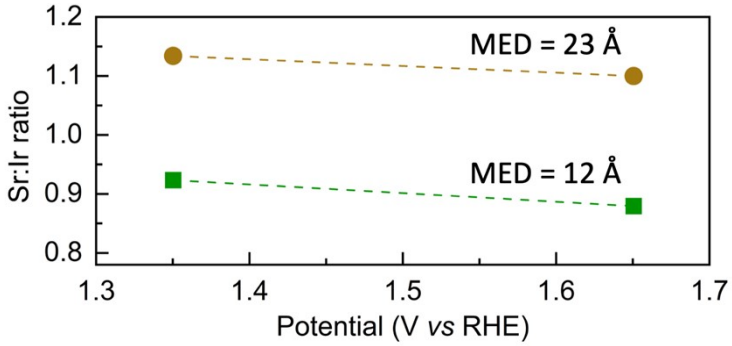

Figure S17. The Sr:Ir ratio after the test in 0.05M $Sr(OH)_2$. This ratio does not fall below 0.86 after a 5-min potentiostatic test at 1.65 V vs RHE (the sample was flushed 5 times with deionized water before the XPS measurement to remove any Sr residuals from the electrolyte)